

Vector magnetocardiography measurement with a compact elliptically polarized laser-pumped magnetometer

WENQIANG ZHENG, SHENGRAN SU, GUOYI ZHANG, XIN BI, AND QIANG LIN*

Collaborative Innovation Center for Bio-Med Physics Information Technology, College of Science, Zhejiang University of Technology, Hangzhou 310023, China

*qlin@zjut.edu.cn

Abstract: We report on a practical approach to vector biomagnetism measurement with an optically pumped magnetometer for measuring total magnetic field intensity. Its application to vector magnetocardiography is experimentally demonstrated with a compact elliptically polarized laser-pumped M_x atomic magnetometer (EPMx OPM). The approach is proved to be effective and able to provide more complete cardiac magnetic information. The cardiac magnetic vectors are displayed in three-dimensional space in the form of magnetic vector loops. The sensor configuration and the image processing method here are expected to form further values, especially for multi-channel vector biomagnetism measurement, clinical diagnosis, and field source reconstruction.

© 2020 Optical Society of America under the terms of the [OSA Open Access Publishing Agreement](#)

1. Introduction

The magnetic fields generated by different organs of the human body often convey valuable information about its source. Therefore, the measurement of human biomagnetism is significant to basic and clinical medicine [1]. A great deal of effort has been contributed to this topic, with major areas of interest being the magnetic fields of the human heart (magnetocardiography, MCG) [2–6], brain (magnetoencephalography, MEG) [7], lung (magnetopneumography, MPG) [8] and eye [9].

MCG, in particular, has received a growing attention as a contactless, non-invasive method for myocardium examination. Unlike the clinically used electric counterpart of body surface potential measurement (electrocardiography, ECG), magnetic signals are characterized by both intensity and direction information. Besides, the transmission of magnetic signal from heart is not affected by the variability of human skin conductance [10–12]. These distinct advantages make MCG a very promising diagnostic technique especially for determining lesion localization, corresponding to the inverse problem of reconstructing the field sources from MCG maps. Though the earliest recognizable measurement of MCG was achieved with multi-turn coils [13], induction-coil-based MCG measurement is difficult to get a significant progress due to poor signal-to-noise ratios of sensors. With the combination of superconducting technology and magnetic field detecting coils, the superconducting quantum interference device (SQUID) was invented. SQUID possesses very prominent sensitivity in the relevant frequency range for MCG. At present, there have been commercial equipments for MCG based on SQUID technique [14], which have made great contributions to the development of MCG research [15,16]. However, SQUID magnetometers require cryogenic cooling, making the installation and maintenance costs too high. Moreover, the liquid-helium-cooled dewar restricts the distance between the skin and sensor and thus reduces the magnetic signal strength. These technical limitations hinder the clinical spread of SQUID-based MCG. The emergence of optically pumped magnetometers (OPMs), which are characterized by laser-based atomic techniques [17], provides a novel means to the development

of MCG measurements [18–22]. Nowadays, sensitivity of OPMs has approached and even exceeded SQUID magnetometers in the laboratory, without the requirement of cryogenics [23,24]. Therefore OPM is widely regarded as a most promising alternative to the SQUID magnetometer. In principle, a number of OPMs record magnetic field information by measuring the Larmor precession frequency of atomic spins. Thus they essentially measure the magnitude of the total magnetic field. This feature makes the way of OPM application very different from the intrinsically vector magnetometer, such as SQUID magnetometer, fluxgate magnetometer [25] and magnetoimpedance magnetometer [26], which are sensitive to one of the three components of the magnetic field vector. To achieve a complete vector magnetocardiography (VMCG) measurement with vector magnetometers, we usually arrange three adjacent sensors, respectively recording the magnetic field component in one direction. However, the magnetic field from heart is not spatially uniform, so the accuracy of the reconstructed field is affected by the separation of sensors. We can also alternate the measurement directions by rotating a single sensor head to realize VMCG. Such mechanical operations complicate the MCG device and still introduce uncertainty to the measurement results. In addition, both methods are operationally difficult especially in terms of designing a multi-channel VMCG device. Various methods exist for realizing the conversion between the scalar and vector modes of an OPM. As typical examples, we can gain vector information by using multiple circularly polarized laser beams [27], or utilizing the ac Stark shift induced by a circularly polarized laser beam [28], or extracting additional information from the first harmonic of the Larmor frequency of an atomic alignment [29], or compensating the measured field [30,31], or exploiting the dependence of electromagnetically induced transparency resonance amplitudes on the external magnetic field direction [32].

In the present paper we propose an approach to VMCG with an OPM, unlike previous work, based upon the fact that cardiac magnetic field is four or five orders of magnitude smaller than the bias magnetic field required to run the OPM. The experiment of VMCG measurement is demonstrated with a compact OPM sensor head. The sensor head is an integrated version of the elliptically polarized laser-pumped M_x atomic magnetometer (EPMx OPM), which has been investigated deeply in our previous work [33]. The EPMx OPM is an improved M_x type OPM, which has been considered as a suitable configuration for MCG measurement [18–21,34]. We achieved VMCG measurements by simply changing the direction of the bias magnetic field. VMCG diagrams from a healthy test male were recorded at different sites above the chest. Some noteworthy findings from VMCG diagrams are reported. Also provided is a visual representation of VMCG, named as magnetic vector loop (MVL). We propose a potential cardiac diagnostic indicator by fitting the MVL plane and extracting the orientation information.

2. Sensor design and principle

2.1. Compact EPMx configuration

The picture of the sensor head module, as well as its design, are depicted in Fig. 1. The length of the module is about 10 cm. The housing is fabricated out of photosensitive resin using 3D printing. Our EPMx OPM used a $20 \times 20 \times 20$ mm uncoated cubic cell, which contains a drop of enriched ^{87}Rb atoms and 200 Torr of N_2 gas for quenching and slowing atomic diffusion. The pressure of N_2 gas gives a cross-talk free distance of ^{87}Rb atoms less than 0.8 mm even at 100 °C [35] and thereby makes the diffusion negligible. The T_2 relaxation time is about 40 ms. A pair of copper heating wire is wound around the cell. When the OPM works, the cell is heated to 45 °C by alternating current at 70 kHz, which is much higher than the atomic resonance frequency to avoid noise caused by heating. Then the temperature is stabilized in a small range of less than 0.1 °C by a closed-loop circuit. The main magnetic field B_0 and the radio-frequency (RF) magnetic field B_{rf} are provided by external coils.

Light from an extended-cavity diode laser, tuned close to ^{87}Rb D1 transition at 795 nm, is delivered into the sensor module via a single-mode polarization-maintaining optical fiber and

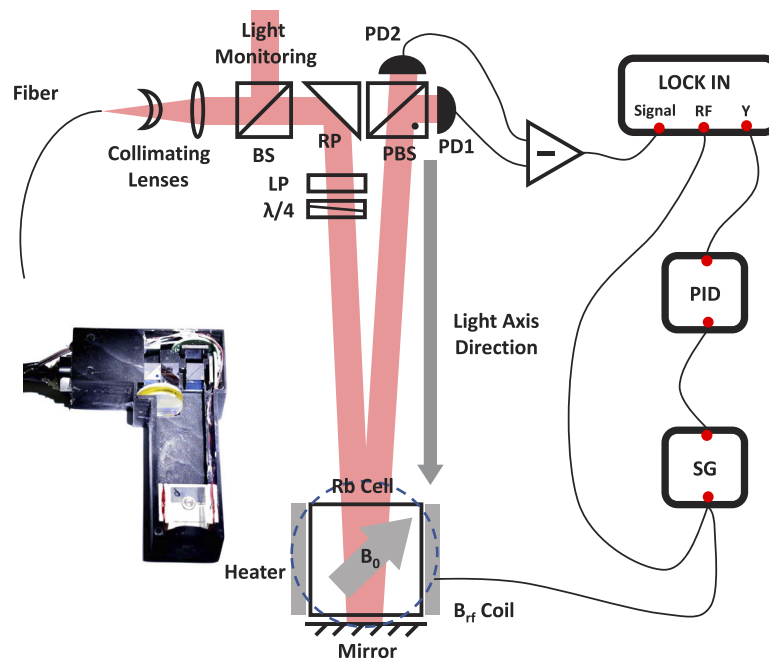


Fig. 1. Schematic diagram and photograph of the magnetometer sensor. BS: beam splitter, RP: right angle reflective prism, PBS: polarized beam splitter, PD: photodiode, LP: linear polarizer, $\lambda/4$: quarter-wave plate, SG: signal generator. B_0 is the constant bias magnetic field. B_{rf} coil is used to generate an oscillating magnetic field B_{rf} which is perpendicular to B_0 .

the beam is expanded to a diameter of about 6 mm by collimating lenses. Then the light is divided into two parts by a beam splitting prism. The reflection part is used to monitor the light parameters, such as frequency, intensity and polarization, so as to provide an optimized optical condition for the sensor. The transmitted light is reflected by the right-angle prism, then the polarization is purified by a linear polarizer. Before illuminating the cell, the light passes through a quarter-wave plate with its optic axis oriented at an angle φ relative to the linear polarizer. The ellipticity of the light can be adjusted by changing the angle φ . The ellipticity can be characterized by the average photon spin $s = \sin(2\varphi)$. It ranges from -1 to +1, where $s = -1(+1)$ corresponds to right (left)-circularly polarized light and $s = 0$ corresponds to linearly polarized light. According to our previous optimization work [33], the optimal φ is about 20 degrees, the optimal laser frequency detuning is about 3 GHz from the transition between the ground state $F = 2$ to the excited state $F' = 1$, and the incident light power is 100 μW . The transmitted light is then reflected back at a small angle less than 7° by a zero degree mirror, which is placed very close to the cell. The structure of such a design allows the vapor cell to be as close as possible to the chest surface while measuring MCG, and also double the length of the optical path, thereby increasing the signal to noise ratio (SNR). When elliptically polarized light passes through polarized atoms, the polarization plane rotates. This rotation is subsequently converted to an electric signal through a balanced polarimeter, consisting of a PBS, two photodetectors, an I/V converter and a differential circuit. The linear polarizer and the quarter-wave plate are rotated to adjust the output signal of the balanced polarimeter to zero before the sensor works. The oscillating optoelectronic signal is then fed to a digital lock-in amplifier (LIA), whose reference signal is the applied oscillating RF field. The demodulated output is used as error signal for the

following servo system, consisting of a proportional-integral-differential (PID) module and a frequency-controlled signal generator.

2.2. Principle of operation

As shown in Fig. 1, the total field \vec{B} contains a main magnetic field \vec{B}_0 and a radio frequency field \vec{B}_{rf} . \vec{B}_{rf} is perpendicular to the plane composed of \vec{B} and the propagation direction of light. The overall evolution of the atomic spin angular momentum \vec{S} is well-described by the Bloch equation [34]

$$\frac{d\vec{S}}{dt} = \gamma \cdot \vec{S} \times \vec{B} + \Gamma_P \cdot (\vec{S}_0 - \vec{S}) - \Gamma_{rel} \cdot \vec{S} \quad (1)$$

Where $\gamma = 7 \text{ Hz/nT}$ is the gyromagnetic ratio of ^{87}Rb atomic spins, Γ_P is the pumping rate, \vec{S}_0 is the equilibrium atomic spin angular momentum in the absence of the oscillating excitation and Γ_{rel} is the spin-relaxation rate. Through the steady-state solution to Eq. (1) in the rotating frame with angular frequency ω_{rf} , which is the oscillating frequency of \vec{B}_{rf} , we can obtain the quadrature amplitude P_{qu} and in-phase amplitude P_{ip} of the photocurrent with respect to the oscillating magnetic field \vec{B}_{rf} , which are given by

$$P_{qu}(\delta) = P_0 \sin(2\vartheta) \frac{\Omega \Gamma_2}{\Omega^2 \Gamma_2 / \Gamma_1 + \Gamma_2^2 + \delta^2}, \quad (2)$$

$$P_{ip}(\delta) = P_0 \sin(2\vartheta) \frac{\delta \Omega}{\Omega^2 \Gamma_2 / \Gamma_1 + \Gamma_2^2 + \delta^2}. \quad (3)$$

Here ϑ is the angle between the direction of laser beam and \vec{B}_0 , Ω is the Rabi frequency, $\delta = \omega_{rf} - \gamma B_0$ is the detuning of the oscillating field B_{rf} from the Larmor frequency, $\Gamma_{1(2)} = \Gamma_{rel}^{1(2)} + \Gamma_P$ is the effective longitudinal (transverse) polarization-relaxation rate. Note that the symbol without an arrow superscript represents the magnitude of the related vector in this paper.

The EPMx OPM is operated in a phase-locked mode, by controlling the driving frequency ω_{rf} . P_{qu} and P_{ip} correspond to the X and Y outputs of the LIA. From Eq. (3), we can see that the Y output is zero if the system is in resonance ($\delta = 0$). Therefore the Y output can be treated as an error signal, based on which the digital PID module adjusts the output frequency of the signal generator. The servo loop thus ensures that the instantaneous Larmor precession frequency of the atomic moments is always in resonance with the driving frequency ω_{rf} . The value of B_0 can be determined from ω_{rf} , as

$$B_0 = \frac{\omega_{rf}}{\gamma}. \quad (4)$$

3. VMCG measurement

3.1. Weak magnetic field measurement in a finite bias magnetic field

As shown in Fig. 2, assume that the bias magnetic field is \vec{B}_0 , and the weak magnetic field to be measured is \vec{B}' . Decomposing \vec{B}' into \vec{B}_{\parallel} (parallel to \vec{B}_0) and \vec{B}_{\perp} (perpendicular to \vec{B}_0), we have

$$\begin{aligned} B - B_0 &= \sqrt{(B_0 + B_{\parallel})^2 + B_{\perp}^2} - B_0 \\ &= \frac{\left(\sqrt{(B_0 + B_{\parallel})^2 + B_{\perp}^2} - B_0 \right) \left(\sqrt{(B_0 + B_{\parallel})^2 + B_{\perp}^2} + B_0 \right)}{\sqrt{(B_0 + B_{\parallel})^2 + B_{\perp}^2} + B_0} \\ &= \frac{B_{\parallel}^2 + B_{\perp}^2 + 2B_{\parallel}B_0}{\sqrt{(B_0 + B_{\parallel})^2 + B_{\perp}^2} + B_0} \end{aligned} \quad (5)$$

Under the condition $B' \ll B_0$, ignoring the quadratic terms B_{\parallel}^2 and B_{\perp}^2 , we have

$$\frac{B_{\parallel}^2 + B_{\perp}^2 + 2B_{\parallel}B_0}{\sqrt{(B_0 + B_{\parallel})^2 + B_{\perp}^2 + B_0}} \approx B_{\parallel}. \quad (6)$$

So Eq. (5) can be simplified to

$$B \approx B_0 + B_{\parallel}. \quad (7)$$

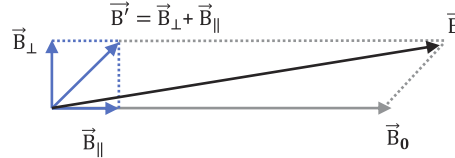


Fig. 2. Schematic diagram of measuring a weak magnetic field \vec{B}' in a much larger bias magnetic field \vec{B}_0 .

In the MCG measurement, B_0 is of the order of 1000 nT, while the cardiac magnetic field B_{heart} is less than 100 pT. The approximation error of Eq. (7) is less than 10 fT, which is negligible compared with the magnitude of B_{heart} . Therefore, Eq. (7) implies an approach to realize vector measurement with a scalar magnetometer. Though the EPMx OPM we used intrinsically measures the magnitude of the total magnetic field, the change in the measurement result actually corresponds to the projection of B_{heart} into the direction of the much larger bias magnetic field. For a complete VMCG, we can sequentially change the direction of the bias magnetic field within three orthogonal axes, named as x, y, and z axis, respectively. It is worth mentioning that the angle between the light beam and the bias field has no influence on the validity of Eq. (7). Therefore, though the bias field has different directions with respect to the incident light beam and to the reflected one in our configuration, the sensitive direction of the sensor is still determined by the bias field. According to Eq. (2) and (3), the small angle between the incident and reflected beams would slight affect the signal amplitude, and such influence on the sensor sensitivity can be ignored.

3.2. VMCG experiment

Now, we turn to experimental demonstration of the VMCG measurement. A healthy male of 30 years old was tested in our experiment. As shown in Fig. 3, the man was sent to a $5 \times \mu$ -metal cylindrical magnetic shield by a slideable bed. The inner diameter of the cylindrical shield is 80 cm, and the length is 200 cm. One end of the cylindrical shield is open. The residual magnetic field in the center of the cylindrical shield is less than 20 nT. Three pairs of orthogonal internal coils are mounted on the inwall of the cylindrical shield for generating the required magnetic bias fields and RF magnetic fields. From Eq. (2) and (3), we can see that a deviation of the light propagation direction from B_0 is a necessary condition to run an EPMx OPM. The coordinate system used in this paper is shown at the upper right of Fig. 3. The sensor head is tilted along the vector direction $(-1, 1, -1)$, so that the light axis is at the same angle to \vec{B}_0 , regardless of which axis is aligned with the bias field. Thus, such configuration enables magnetic field measurement in three directions. A commercial current source (B2912A from Keysight) is used to supply a stable and well-defined bias field of about 1000 nT. As shown in Fig. 4, through the optimization process described in Ref. [33], sensitivities of around 300 fT/ $\sqrt{\text{Hz}}$ are achieved at the temperature of 45 °C in all of the three mutually orthogonal directions, which have approached to the limit set by the noise level of the current source. Assisted by a separate test coil, we determined that the bandwidth of the sensor is about 100 Hz, which has met the requirement for MCG measurements.

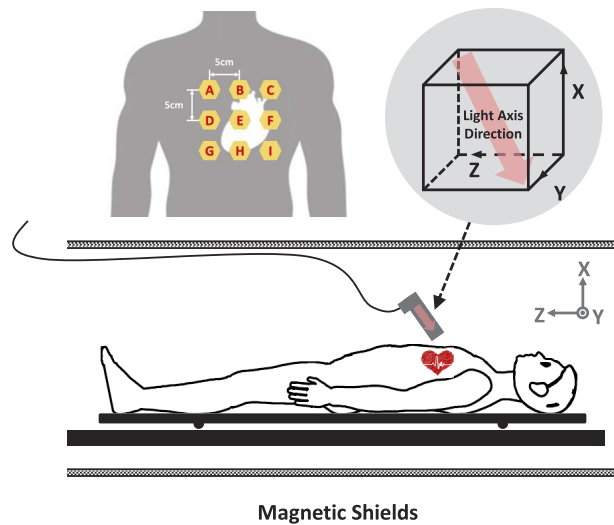


Fig. 3. Schematic diagram of VMCG measurement. The tested male was pushed into a 5-layer permalloy cylindrical magnetic shield by a slideable bed. One end of the cylindrical shield was open. The sensor head was attached to a three-dimensionally movable holder. The optical axis direction is displayed at the upper right. A total of 9 sites above the chest were selected for VMCG measurements.

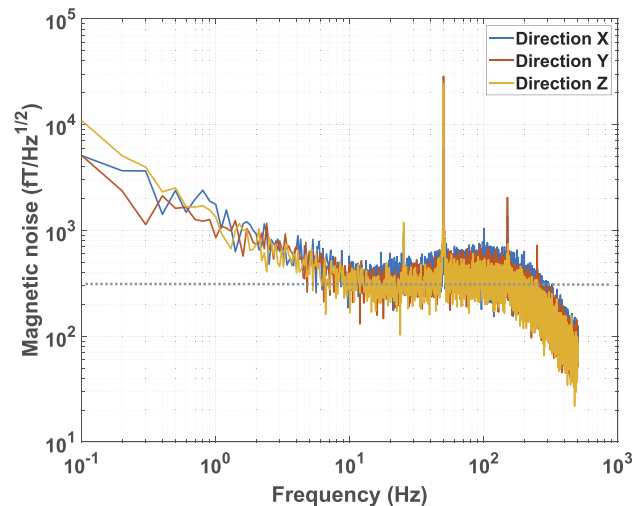


Fig. 4. Measured sensitivity of the magnetometer in three directions. The dotted line indicates a sensitivity of 300 fT/√Hz.

As shown in Fig. 3, 3×3 sites above the chest were selected for VMCG measurements. These sites were spaced 5 cm apart. The VMCG measurement at each site was achieved by changing the direction of the bias magnetic field \vec{B}_0 and the RF field \vec{B}_{rf} . So there was no need to move the human body or the sensor. The working parameters were automatically searched by a software program based on MATLAB. When we changed the magnetic field strength or started the measurement at a new site, the software program automatically scanned the driving frequency in open loop mode to determine the Larmor frequency and gave proper PID parameters. The

initialization process took approximately 30 seconds. The signals of 20 heartbeat cycles were collected in each direction, so the measurement time for each site took about 1 minute. During the MCG measurement, a reference signal was also synchronously acquired by a simple ECG device. The ECG signal allows for improving the SNR in an off-line averaging and distinguishing the periods of different cardiac activities.

4. Experimental results and discussion

Figure 5 shows a real-time MCG signal acquired in the x direction at site B, as well as its reference ECG signal. A digital band-stop filter centered at 50 Hz was used to suppress power frequency noise. The ECG signals served as timing reference for distinguishing the individual heart beats when averaging. Averaged MCG signals (20 beats) of all sites at different directions are presented in Fig. 6. It is interesting to find that the MCG signals show specific waveform in different directions, even at the same site. For example, at site A, the P wave and T wave are opposite in phase in the x and z directions, while they are inphase in the y direction. There also is much difference in signal strengths between different directions. At site D and E, P waves appear only when we measure MCG in x direction. At site G, T wave is obvious in x direction. Besides, the MCG waveforms show high dependencies on the measurement position. At site I, we can get clear U waves.

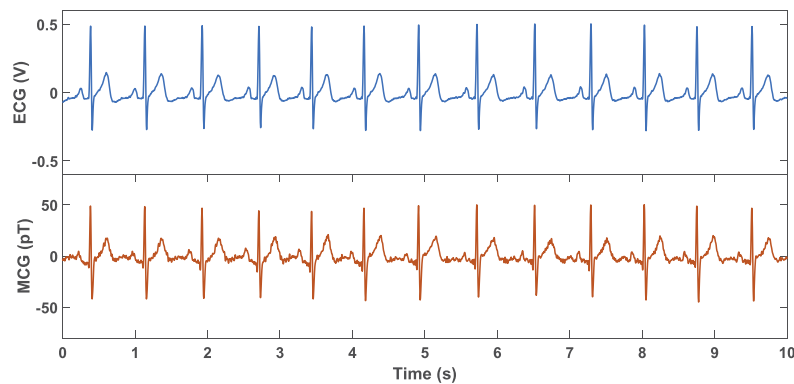


Fig. 5. Real-time cardiac signals of the tested male detected simultaneously with ECG electrodes (blue) and the EPMx OPM (red).

In order to clearly show the spatial characteristics of the heart magnetic field, we synthesize the MCG signals in x, y and z directions into a magnetic field vector and display it as a MVL map. Specifically, MVL map is the trajectory of the end of the cardiac magnetic vector in three-dimensional space in a heartbeat cycle. Fig. 7 shows the synthesis of MVL map for site A. The periods of different cardiac activities are determined by ECG signals and are marked with different colors. We can see that MVL map can visually display the changing process of the cardiac magnetic field direction during a heartbeat cycle. This is difficult to achieve with traditional MCG images. In addition, P, QRS, and T waves can be clearly distinguished, as they form different vector rings. The loops related to different cardiac activities are very different in shapes, plane orientations and enclosed areas. The orientations of QRS loop and T loop are roughly the same. It is understandable since they both correspond to the electrophysiological activity of the ventricles, while P loop corresponds to the electrophysiological activity of the atria. The enclosed areas of loops are determined by both durations and intensities of corresponding electrophysiological activities.

All of the VML maps for 9 sites are presented in Fig. 8(a), from which we can see that the directions and shapes of the loops change significantly with the measurement position. We fitted

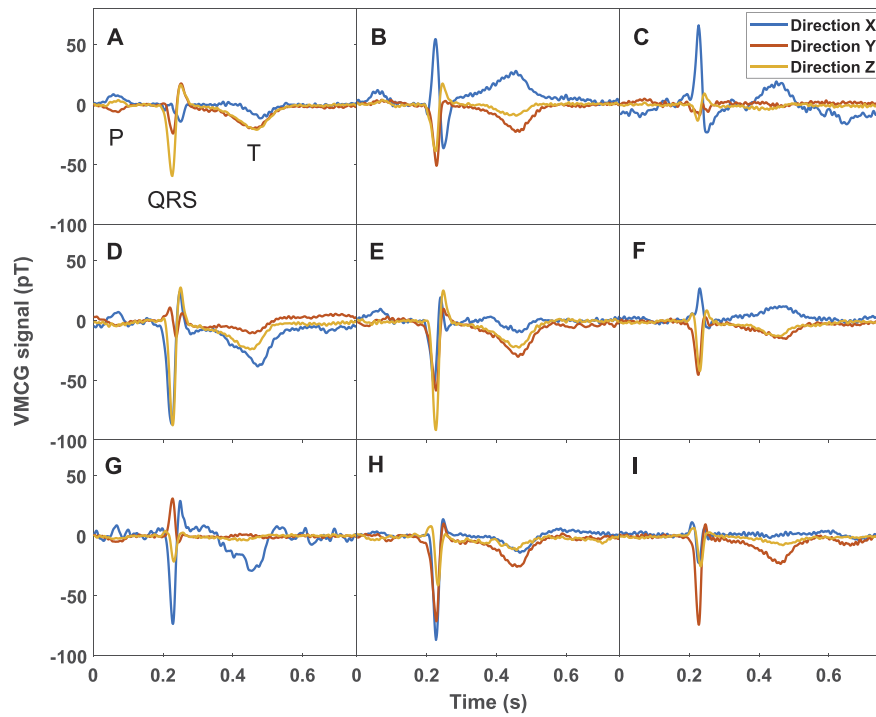


Fig. 6. Averaged MCG signals (20 beats) of all sites at different directions.

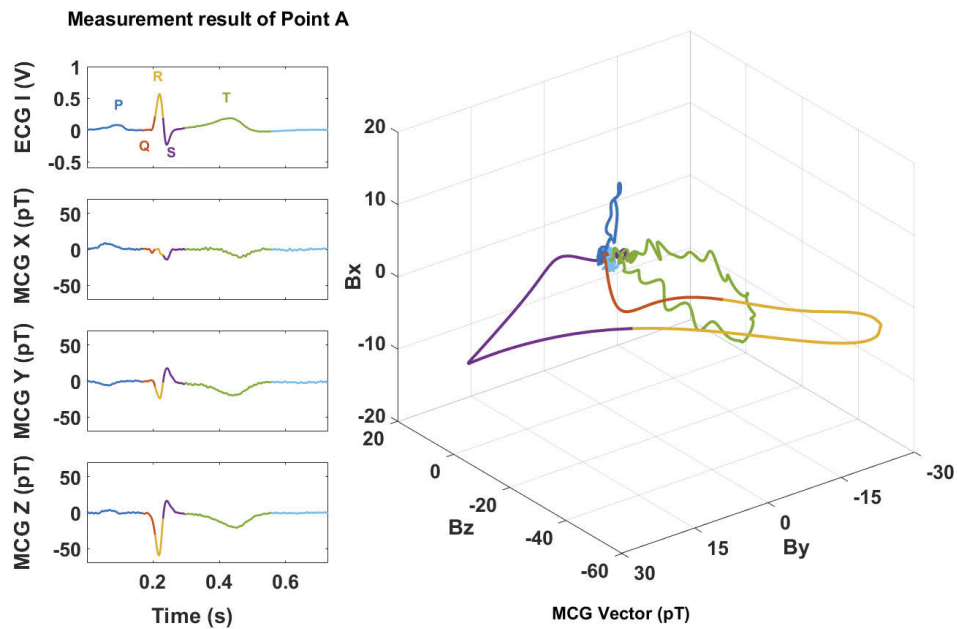
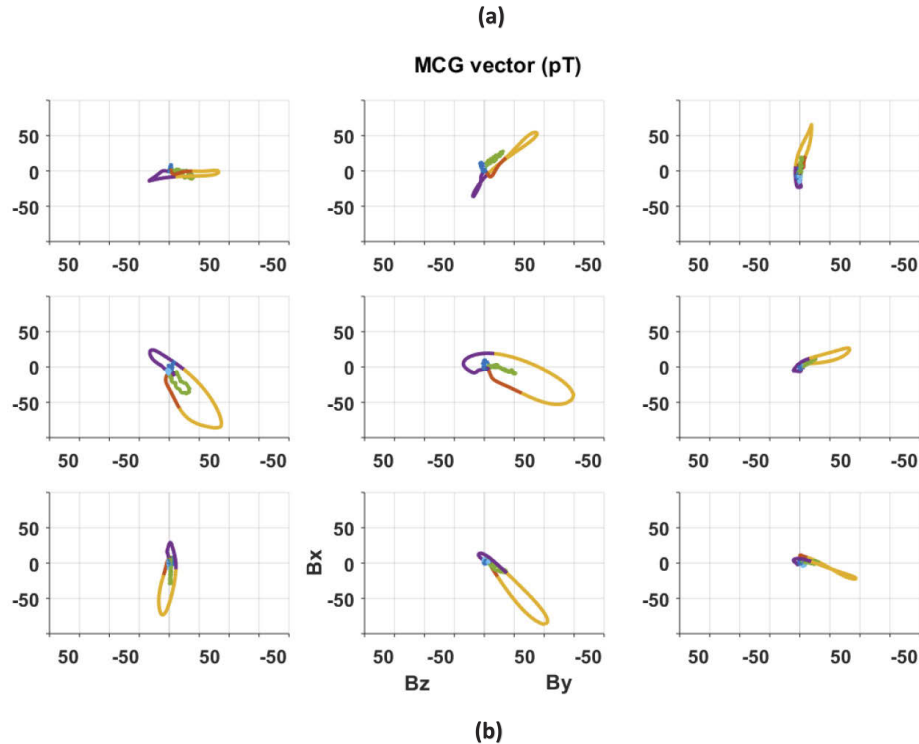


Fig. 7. MVL map synthesis for site A. The left side is the ECG signal and the MCG signals in different directions. For the sake of distinction, P, QRS, and T waves are marked with different colors. The right side is the corresponding MVL map.

each vector loop with two-dimensional plane parameters and got the corresponding characteristic plane. The principal axes and normal vectors of these planes for QRS (T) waves are presented as v-QRS (T) and n-QRS (T) in Fig. 8(b), respectively. The average of angles between the QRS plane and the T plane is 18.49 degrees with a standard deviation of 6.75 degrees.



	n-QRS	v-QRS (pT)	n-T	v-T (pT)
A	(-0.23,-0.87,0.44)	(-1.01,-23.56,-59.35)	(-0.23,-0.67,0.7)	(-8.81,-19.44,-20.84)
B	(0.41,-0.21,0.89)	(53.96,-49.36,-38.47)	(0.35,-0.08,0.93)	(28.09,-22.52,-9.09)
C	(0.17,0.12,0.98)	(66.04,-7.38,-11.99)	(0.13,0.63,0.76)	(19.29,0.54,-3.16)
D	(-0.49,-0.72,0.49)	(-85.42,3.29,-86.8)	(-0.17,-0.75,0.64)	(-35.43,-10.22,-23.42)
E	(0,-0.84,0.54)	(-44.39,-56.76,-90.5)	(-0.03,-0.61,0.79)	(-8.83,-29.95,-22.09)
F	(0.79,-0.11,0.61)	(25.94,-42.09,-40.48)	(0.53,-0.16,0.83)	(12.1,-14.28,-12.62)
G	(-0.29,-0.3,0.91)	(-73.28,30.62,-19.95)	(-0.02,0.63,0.77)	(-29.06,1.03,-2.1)
H	(-0.63,0.64,0.45)	(-85.48,-71.1,-31.61)	(0.12,-0.37,0.92)	(-12.15,-25.66,-11.66)
I	(-0.78,0.13,0.62)	(-22.58,-73.96,-18.84)	(0.33,-0.29,0.9)	(1.65,-23.26,-7.14)

Fig. 8. Characterization of VMCG signals. (a) Synthetic VML maps at different measurement positions. The viewing angle is 45 degrees based on the y axis and z axis. (b) Fitted characteristic planes for QRS and T loops. n-QRS (T) denotes the normal vector of the QRS (T) plane. v-QRS (T) denotes the principal axis of the QRS (T) loop, defined as the largest vector from the origin to the trace of the QRS (T) loop.

5. Conclusions

In conclusion, we have presented a practical approach to vector biomagnetic measurements with an OPM, without any need of additional sensors or mechanical rotations of the sensor heads. The approach was experimentally demonstrated by an EPMx OPM based on ^{87}Rb atoms. We gained VMCG maps from 9 sites above the chest of a healthy male. The results verify that the waveforms and strengths of VMCG are highly dependent on the measurement positions and directions. It is very different from the ECG lead, which essentially measures the potential difference between two sites. Moreover, we show that more information about the characteristics of VMCG signals can be extracted by fitting the MVL maps. Actually, VMCG is a comprehensive result of the biological currents from all cardiac cells. When some myocardial cells are abnormal during a heartbeat cycle, such as in the situation of bundle branch block or myocardial infarction, direction and intensity anomalies of the cardiac magnetic vector may happen. We expect that such anomalies can form diagnostic basis by observing the directions or shapes of the VML maps.

This work enables OPMs for measuring total magnetic field intensity to have new development potential in the measurement of vector biomagnetism. It provides a suitable tool for the further realization of multi-channel VMCG measurements. VMCG conveys unique information about the heart condition, which is important for the cardiac diagnosis and the source inversion problem. To explore the value of VMCG technique, there is still much work to be done in developing multi-channel vector magnetic detection sensor and performing more clinical analysis.

Funding

National Basic Research Program of China (973 Program) (2017YFC0601602); National Natural Science Foundation of China (11605153, 61475139, 61727821); Natural Science Foundation of Zhejiang Province (LY20A050003).

Disclosures

The authors declare no conflicts of interest.

References

1. W. Andrä and H. Nowak, *Magnetism in Medicine: A Handbook* (John Wiley & Sons, 2007).
2. S. Watanabe and S. Yamada, "Magnetocardiography in early detection of electromagnetic abnormality in ischemic heart disease," *J. Arrhythmia* **24**(1), 4–17 (2008).
3. S. Yamada and I. Yamaguchi, "Magnetocardiograms in clinical medicine: unique information on cardiac ischemia, arrhythmias, and fetal diagnosis," *Intern. Med.* **44**(1), 1–19 (2005).
4. P. J. Karp, T. E. Katila, M. Saarinen, P. Siltanen, and T. T. Varpula, "The normal human magnetocardiogram. II. A multipole analysis," *Circ. Res.* **47**(1), 117–130 (1980).
5. R. R. Fenici, M. Masselli, L. Lopez, and G. Melillo, "Clinical value of magnetocardiography," in *Electrocardiography and Cardiac Drug Therapy* (Springer, 1989), pp. 239–258.
6. H. Horigome, K. Ogata, A. Kandori, T. Miyashita, M. Takahashi-Igari, Y.-J. Chen, H. Hamada, and K. Tsukada, "Standardization of the PQRS waveform and analysis of arrhythmias in the fetus using vector magnetocardiography," *Pediatr. Res.* **59**(1), 121–125 (2006).
7. E. Boto, N. Holmes, J. Leggett, G. Roberts, V. Shah, S. S. Meyer, L. D. Muñoz, K. J. Mullinger, T. M. Tierney, S. Bestmann, G. R. Barnes, R. Bowtell, and M. J. Brookes, "Moving magnetoencephalography towards real-world applications with a wearable system," *Nature* **555**(7698), 657–661 (2018).
8. J. Tomek, A. Platil, P. Ripka, and P. Kaspar, "Application of fluxgate gradiometer in magnetopneumography," *Sens. Actuators, A* **132**(1), 214–217 (2006).
9. A. Antervo, R. Hari, T. Katila, T. Ryhänen, and M. Seppänen, "Magnetic fields produced by eye blinking," *Electroencephalogr. Clin. Neurophysiol.* **61**(4), 247–253 (1985).
10. R. Fenici, D. Brisinda, and A. M. Meloni, "Clinical application of magnetocardiography," *Expert Rev. Mol. Diagn.* **5**(3), 291–313 (2005).
11. V. Mäntynen, T. Konttila, and M. Stenroos, "Investigations of sensitivity and resolution of ECG and MCG in a realistically shaped thorax model," *Phys. Med. Biol.* **59**(23), 7141–7158 (2014).

12. J.-W. Park, E.-S. Shin, S. H. Ann, M. Gödde, L. S.-I. Park, J. Brachmann, S. Vidal-Lopez, J. Wierzbinski, Y.-Y. Lam, and F. Jung, "Validation of magnetocardiography versus fractional flow reserve for detection of coronary artery disease," *Clin. Hemorheol. Microcirc.* **59**(3), 267–281 (2015).
13. G. M. Baule, "Detection of the magnetic field of the heart," *Am. Heart J.* **66**(1), 95–96 (1963).
14. U. Steinhoff, A. Schnabel, M. Burghoff, T. Freibier, F. Thiel, H. Koch, and L. Trahms, "Spatial distribution of cardiac magnetic vector fields acquired from 3120 SQUID positions," *Neurol. Clin. Neurophysiol.* **59**, 1–6 (2004).
15. W. H. Barry, W. M. Fairbank, D. C. Harrison, K. L. Lehrman, J. A. Malmivuo, and J. P. Wikswo, "Measurement of the human magnetic heart vector," *Science* **198**(4322), 1159–1162 (1977).
16. L. A. Bradshaw, J. K. Ladipo, D. J. Staton, J. P. Wikswo, and W. O. Richards, "The human vector magnetogastrogram and magnetoenterogram," *IEEE Trans. Biomed. Eng.* **46**(8), 959–970 (1999).
17. D. Budker and M. Romalis, "Optical magnetometry," *Nat. Phys.* **3**(4), 227–234 (2007).
18. G. Lembke, S. N. Ern , H. Nowak, B. Menhorn, A. Pasquarelli, and G. Bison, "Optical multichannel room temperature magnetic field imaging system for clinical application," *Biomed. Opt. Express* **5**(3), 876–881 (2014).
19. A. Weis, "Optically pumped alkali magnetometers for biomedical applications," *Europhys. News* **43**(3), 20–23 (2012).
20. G. Bison, N. Castagna, A. Hofer, P. Knowles, J. L. Schenker, M. Kasprzak, H. Saudan, and A. Weis, "A room temperature 19-channel magnetic field mapping device for cardiac signals," *Appl. Phys. Lett.* **95**(17), 173701 (2009).
21. G. Bison, R. Wynands, and A. Weis, "A laser-pumped magnetometer for the mapping of human cardiomagnetic fields," *Appl. Phys.* **76**(3), 325–328 (2003).
22. R. Wyllie, M. Kauer, G. Smetana, R. Wakai, and T. Walker, "Magnetocardiography with a modular spin-exchange relaxation-free atomic magnetometer array," *Phys. Med. Biol.* **57**(9), 2619–2632 (2012).
23. H. B. Dang, A. C. Maloof, and M. V. Romalis, "Ultra-high sensitivity magnetic field and magnetization measurements with an atomic magnetometer," *Appl. Phys. Lett.* **97**(15), 151110 (2010).
24. D. Sheng, S. Li, N. Dural, and M. V. Romalis, "Subfemtotesla scalar atomic magnetometry using multipass cells," *Phys. Rev. Lett.* **110**(16), 160802 (2013).
25. N. Gusev, P. Vetoshko, A. Kuzmichev, D. Chepurnova, E. Samoilova, A. Zvezdin, A. Korotaeva, and V. Belotelov, "Ultra-Sensitive Vector Magnetometer for Magnetocardiographic Mapping," *Biomed. Eng.* **51**(3), 157–161 (2017).
26. T. Takiya and T. Uchiyama, "Development of active shielding-type MI gradiometer and application for magnetocardiography," *IEEE Trans. Magn.* **53**(11), 1–4 (2017).
27. S. Afach, G. Ban, G. Bison, K. Bodek, Z. Chowdhuri, Z. D. Grujić, L. Hayen, V. H laine, M. Kasprzak, and K. Kirchet al., "Highly stable atomic vector magnetometer based on free spin precession," *Opt. Express* **23**(17), 22108–22115 (2015).
28. B. Patton, E. Zhivun, D. C. Hovde, and D. Budker, "All-optical vector atomic magnetometer," *Phys. Rev. Lett.* **113**(1), 013001 (2014).
29. L. Lenci, A. Auyuanet, S. Barreiro, P. Valente, A. Lezama, and H. Failache, "Vectorial atomic magnetometer based on coherent transients of laser absorption in Rb vapor," *Phys. Rev. A* **89**(4), 043836 (2014).
30. A. Vershovskii, "A new method of absolute measurement of the three components of the magnetic field," *Opt. Spectrosc.* **101**(2), 309–316 (2006).
31. A. Papoyan, S. Shmavonyan, A. Khanbekyan, K. Khanbekyan, C. Marinelli, and E. Mariotti, "Magnetic-field-compensation optical vector magnetometer," *Appl. Opt.* **55**(4), 892–895 (2016).
32. K. Cox, V. I. Yudin, A. V. Taichenachev, I. Novikova, and E. E. Mikhailov, "Measurements of the magnetic field vector using multiple electromagnetically induced transparency resonances in Rb vapor," *Phys. Rev. A* **83**(1), 015801 (2011).
33. S. Su, G. Zhang, X. Bi, X. He, W. Zheng, and Q. Lin, "Elliptically polarized laser-pumped Mx magnetometer towards applications at room temperature," *Opt. Express* **27**(23), 33027–33039 (2019).
34. G. Bison, R. Wynands, and A. Weis, "Optimization and performance of an optical cardiomagnetometer," *J. Opt. Soc. Am. B* **22**(1), 77–87 (2005).
35. K. Kim, S. Begus, H. Xia, S. Lee, V. Jazbinsek, Z. Trontelj, and M. V. Romalis, "Multi-channel atomic magnetometer for magnetoencephalography: A configuration study," *NeuroImage* **89**, 143–151 (2014).